JACS
JOURNAL OF THE AMERICAN CHEMICAL SOCIETY
pubs.acs.org/JACS
Article

Enhanced Nitrate-to-Ammonia Activity on Copper–Nickel Alloys via Tuning of Intermediate Adsorption

Yuhang Wang,[#] Aoni Xu,[#] Ziyun Wang,[#] Linsong Huang, Jun Li, Fengwang Li, Joshua Wicks, Mingchuan Luo, Dae-Hyun Nam, Chih-Shan Tan, Yu Ding, Jiawen Wu, Yanwei Lum, Cao-Thang Dinh, David Sinton, Gengfeng Zheng, and Edward H. Sargent*

Cite This: https://dx.doi.org/10.1021/jacs.9b13347

ABSTRACT: Electrochemical conversion of nitrate (NO_3^-) into ammonia (NH_3) recycles nitrogen and offers a route to the production of NH_3, which is more valuable than dinitrogen gas. However, today's development of NO_3^- electroreduction remains hindered by the lack of a mechanistic picture of how catalyst structure may be tuned to enhance catalytic activity. Here we demonstrate enhanced NO_3^- reduction reaction (NO_3^-RR) performance on $Cu_{50}Ni_{50}$ alloy catalysts, including a 0.12 V upshift in the half-wave potential and a 6-fold increase in activity compared to those obtained with pure Cu at 0 V vs reversible hydrogen electrode (RHE). Ni alloying enables tuning of the Cu *d*-band center and modulates the adsorption energies of intermediates such as $*NO_3^-$, $*NO_2$, and $*NH_2$. Using density functional theory calculations, we identify a NO_3^-RR-to-NH_3 pathway and offer an adsorption energy–activity relationship for the CuNi alloy system. This correlation between catalyst electronic structure and NO_3^-RR activity offers a design platform for further development of NO_3^-RR catalysts.

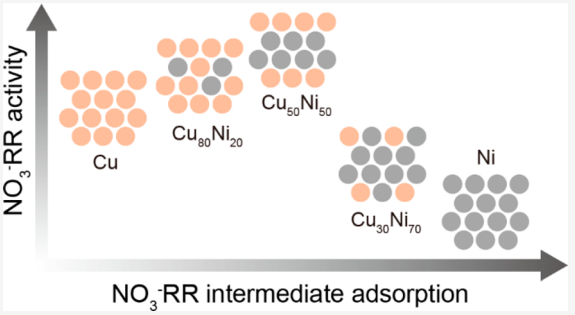

INTRODUCTION

Human activities have led to an anthropogenically induced increase over time in the concentration of environmental NO_3^-:[1,2] the combustion of fossil fuels emits nitrous oxides (NO_x); fertilizer-intensive agriculture releases NO_3^- into soil and groundwater; and NO_3^--containing waste is discharged from industrial sources. The accumulation of NO_3^- induces acid rain and photochemical smog,[3,4] and the uptake of NO_3^- in mammals results in its *in vivo* conversion to nitrite (NO_2^-),[5,6] a cause of methemoglobinemia and a known carcinogen.

Closing the NO_3^-–nitrogen cycle[1,2,7,8] is therefore of interest: it is desirable to transform NO_3^- to harmless[9−11] or, better yet, value-added products.[12,13] The electrochemical reduction of NO_3^- provides a route to the production NH_3,[9,13] which has widespread use as a fertilizer precursor, chemical feedstock, and fuel:[14]

$$NO_3^- + 6H_2O + 8e^- \rightarrow NH_3 + 9OH^-, \quad E^0 = 0.69\ \text{V vs RHE (pH = 14)} \qquad (1)$$

Achieving higher-performance electrocatalysts for NO_3^-RR remains challenging, in significant part because the relationship between catalyst structure and activity is poorly understood.

To date, Faradaic efficiencies (FEs) greater than 90% for NO_3^- reduction to NH_3 have been achieved on Cu-based catalysts, but typically these require potentials more negative than −0.27 V vs RHE in NO_3^--containing 1 M KOH electrolytes, corresponding to an overpotential exceeding 0.96 V.[15−19] Previous studies found that alloying Cu with Ni results in a positive shift in the NO_3^-RR half-wave potential ($E_{1/2}$), the potential at which the current is equal to one-half of the mass-transfer-limiting current, by ∼0.1 V,[18,19] a finding that corresponds to enhanced catalytic activity at a given potential. A mechanism wherein Cu performs the adsorption of NO_3* and Ni is the binding site of H* was proposed by Simpson and Johnson;[20] however, this mechanism does not explain enhanced NO_3^-RR activity on CuNi alloys: Ni converts NO_3^- to NH_3 inefficiently,[19] so replacing surface Cu atoms with Ni would be expected to reduce the density of active sites for NH_3 production.

We noted that upshifts in the half-wave potential ($E_{1/2}$) in reduction reactions typically suggest an increase in electrocatalytic activity. This, we posited, could arise due to a modulated intermediate adsorption energy in CuNi alloys compared to pure Cu. Drawing parallels with oxygen reduction reaction (ORR) literature, we noted that platinum–nickel

Received: December 11, 2019
Published: March 2, 2020

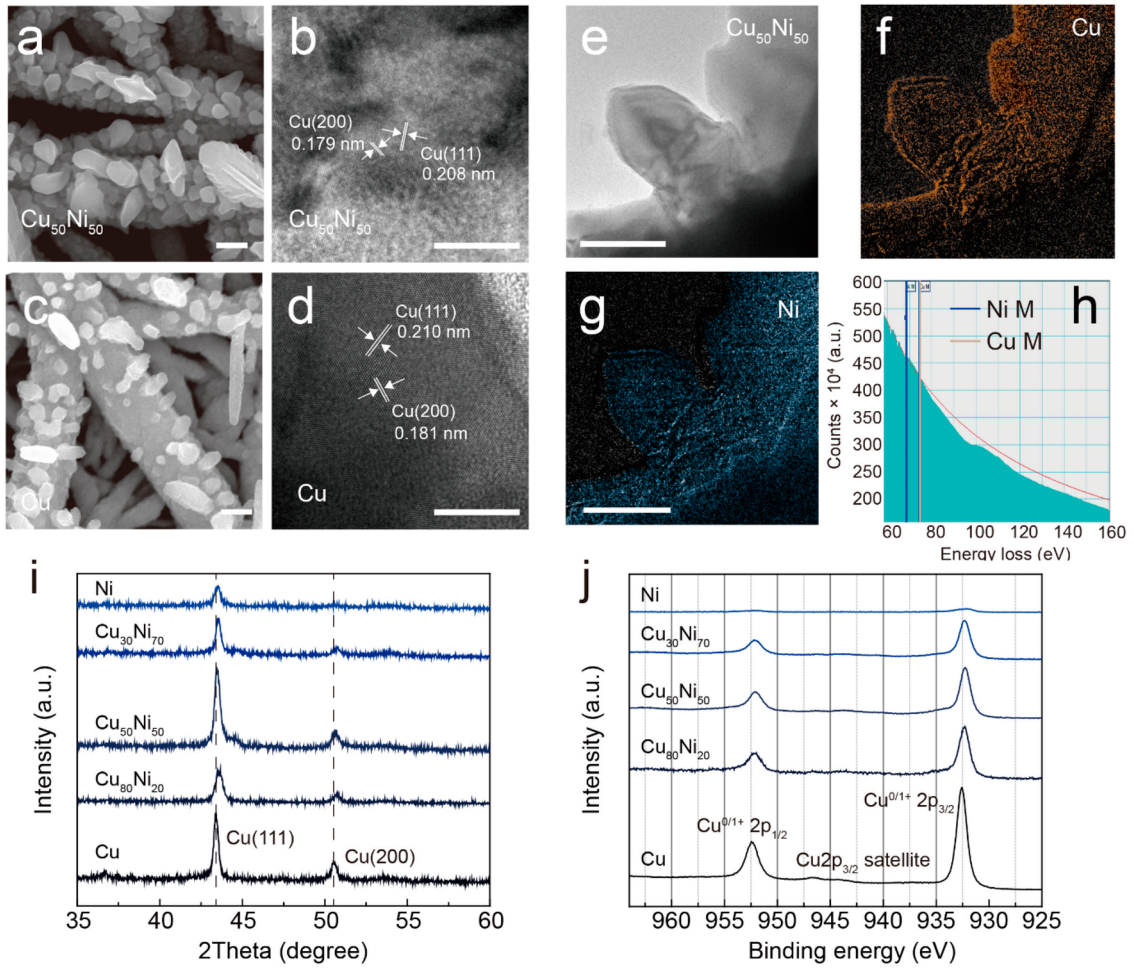

Figure 1. Materials characterization of copper−nickel alloy catalysts. (a, b) Representative SEM and HRTEM images of the $Cu_{50}Ni_{50}$ catalyst. (c, d) Representative SEM and HRTEM images of the pure Cu catalyst. The scale bars are 200 nm in (a) and (c), and 10 nm in (b) and (d). (e−h) STEM image and EELS mapping analysis of the $Cu_{50}Ni_{50}$ catalyst. The scale bars are 100 nm. (i, j) XRD patterns and XPS Cu 2p spectra of catalysts with different Cu:Ni ratios.

(PtNi) alloy catalysts typically exhibit an upshifted half-wave potential of ∼0.1 V compared to pure Pt catalysts.[21,22] Decreasing adsorption energies for oxygenated species on PtNi alloys leads to increased activity, an instance of scaling relations for ORR catalysts.[23] This has been associated with the shifted *d*-band center position and surface atomic arrangement reported by Marković and co-workers.[22]

In sum, the introduction of heteroatoms modulates the electronic structure of catalysts, enabling the enhancement of electrocatalytic activity.[22−25] We explore herein how such a strategy can be employed to design catalysts exhibiting enhanced NO_3^-RR activity and selectivity.

We began by preparing a series of CuNi alloys with various Cu:Ni compositions, and we observed a 0.12 V upshift in $E_{1/2}$ and a 0.2 V lower overpotential required for peak NH_3 FE. This occurred at a composition—$Cu_{50}Ni_{50}$ alloy catalysts—that simultaneously produced a 6-fold increase in NO_3^-RR activity compared to the case of pure Cu at 0 V vs RHE (pH = 14). We utilized X-ray photoelectron spectroscopy (XPS), *operando* X-ray adsorption spectroscopy (XAS), and ultraviolet photoelectron spectroscopy (UPS) to investigate the electronic structure of the catalysts and found that the Cu *d*-band center upshifted toward the Fermi level in CuNi alloys.

In addition, we investigate the reaction pathway with density functional theory (DFT) calculations and build an intermediate adsorption energy−NO_3^-RR performance relationship for the CuNi alloy system.

RESULTS AND DISCUSSION

Catalyst Synthesis and Characterization. We began by electrodepositing catalysts on both rotating disk electrodes (RDEs) and polytetrafluoroethylene (PTFE) membranes covered with a 300 nm thick Cu seed layers (300 nm Cu/PTFE). We used electron microscopy to investigate the morphological and crystalline structure of the catalysts. The CuNi catalysts with Cu-to-Ni ratios of 80:20, 50:50, and 30:70 in the deposition solutions, labeled $Cu_{80}Ni_{20}$, $Cu_{50}Ni_{50}$, and $Cu_{30}Ni_{70}$, exhibited dendritic morphologies (Figure 1a and Figures S1 and S2) with dendrite diameters in the range of 200−400 nm. Using high-resolution transmission electron microscopy (HRTEM), we observed lattice spacings of 0.208 and 0.179 nm for the Cu(111) and Cu(200) facets (Figure 1b) of the $Cu_{50}Ni_{50}$ catalysts due to the formation of the CuNi alloy phase—compared to pure Cu dendrites exhibiting lattice spacings of 0.210 and 0.181 nm for Cu(111) and Cu(200) facets that agree with cubic Cu (Figure 1d).[26] The Cu-to-Ni ratio in the $Cu_{50}Ni_{50}$ catalyst, quantified by electron energy loss

https://dx.doi.org/10.1021/jacs.9b13347
J. Am. Chem. Soc. XXXX, XXX, XXX−XXX

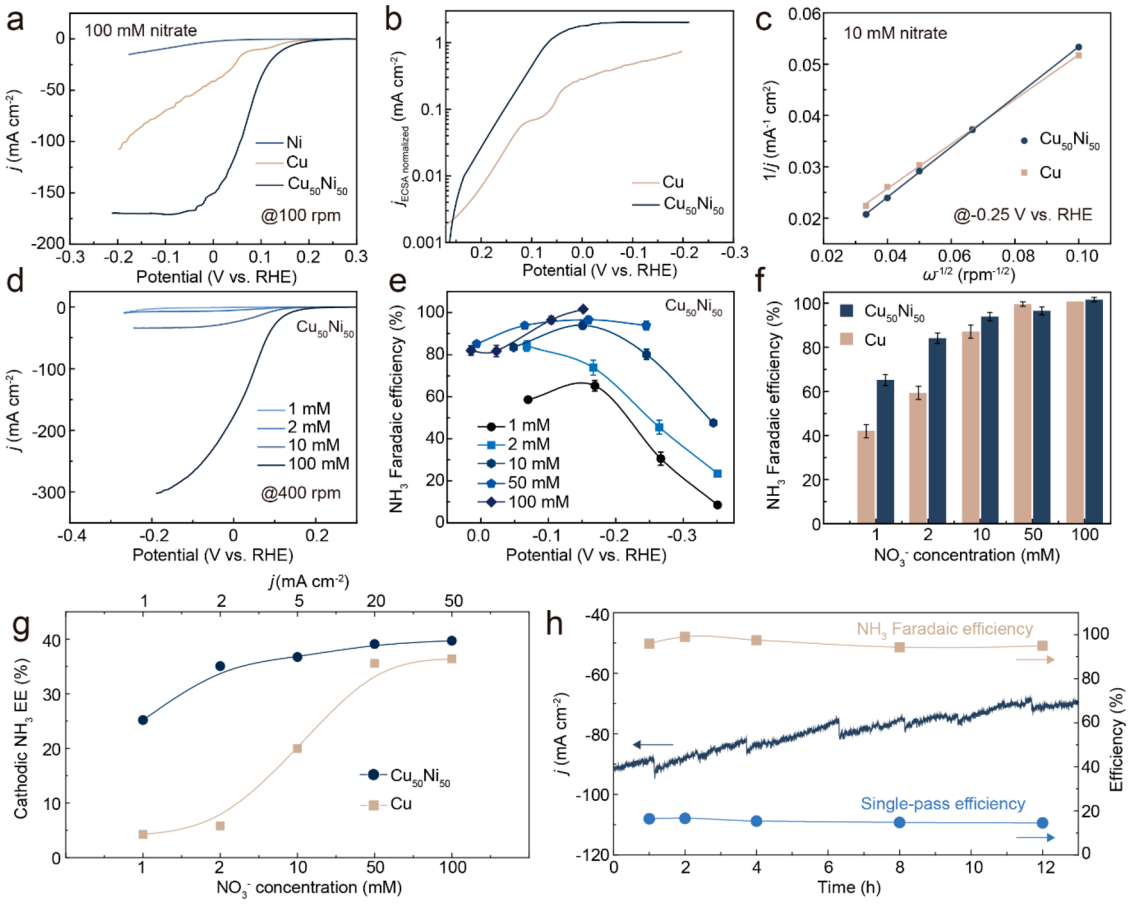

Figure 2. NO_3^--to-NH_3 electroreduction performance. (a) j–V plots of NO_3^- reduction (80% iR corrected) on the $Cu_{50}Ni_{50}$, pure Cu, and pure Ni RDE at 100 rpm in 1 M KOH + 0.1 M KNO_3 electrolyte. (b) ECSA-normalized current densities. (c) Koutecký–Levich plots of NO_3^- reduction on $Cu_{50}Ni_{50}$ and Cu at −0.25 V vs RHE in 1 M KOH + 10 mM KNO_3 electrolyte. (d) j–V plots of NO_3^- reduction (80% iR corrected) on the $Cu_{50}Ni_{50}$ RDE at 400 rpm. (e) NO_3^--to-NH_3 Faradaic efficiency (FE) on the $Cu_{50}Ni_{50}$/PTFE catalyst in different NO_3^- concentrations. (f) Comparison of the highest NH_3 FE on the $Cu_{50}Ni_{50}$/PTFE and pure Cu/PTFE catalysts at different NO_3^- concentrations. (g) Comparison of the cathodic (half-cell) NH_3 energy efficiency (EE) obtained using the $Cu_{50}Ni_{50}$/PTFE and pure Cu/PTFE catalysts. (h) Stability and single-pass conversion test of nitrate reduction at −0.1 V vs RHE using a $Cu_{50}Ni_{50}$/Cu foam catalyst.

spectroscopy (EELS, Figure 1e–h), was ∼52:48. We observed similar ratios at other randomly selected positions (Figure S3 and Table S1), arguing against a main role for catalyst heterogeneity in catalytic performance. X-ray diffraction (XRD) reveals a decrease in Cu lattice spacings when Ni is incorporated (Figure 1i and Figure S4). The Cu(111) and Cu(100) d-spacings of the $Cu_{50}Ni_{50}$ catalyst revealed by XRD agree with the results observed with HRTEM.

We also looked for evidence of changes in the electronic properties of the Cu and Cu:Ni catalysts. XPS indicated a notable decrease in the Cu 2p binding energy and an increase in the metallic Ni 2p binding energy for the alloyed catalysts (Figure 1j and Figure S5). Among the three alloyed catalysts, we found the largest Cu 2p binding energy shift of ∼0.35 eV in $Cu_{50}Ni_{50}$. This can be explained through electron redistribution,[27] which leads to an opposite shift of the Cu 3d band toward the Fermi level,[28] tuning the adsorption energies of both H* and NO_3*.

In the case of the pure Ni catalysts, only the XRD peaks of the Cu/PTFE support were observed (Figure 1i). XPS measurements exhibited a Cu 2p binding energy very similar to that for pristine Cu/PTFE (Figure S6). SEM, elemental mapping, and Ni 2p XPS (Figures S5 and S7) revealed only Ni, accompanied by NiO_x formed by oxidation in air, fully covering the Cu/PTFE fibers.

NO_3^-RR Activity and Kinetics. To investigate the electrocatalytic activity and kinetics of NO_3^- reduction, we tested each catalyst on RDEs. With the $Cu_{50}Ni_{50}$ catalyst, we found an onset potential of ∼0.25 V vs RHE (pH = 14) for NO_3^- reduction (Figure 2a). The current density then increased sharply to its transport-limited ceiling of ∼170 mA cm^{-2} (according to eq 1 in Supporting Information) at 100 rpm in 1 M KOH + 100 mM KNO_3 (pH = 14) electrolyte. On the pure Cu catalysts, we found that a much more negative cathodic potential was required to reach this same NO_3^--transport-limited current: the current density was only 100 mA cm^{-2} at −0.2 V vs RHE, which was only 60% of that obtained by operating the $Cu_{50}Ni_{50}$ catalyst at the same potential. The pure Ni catalyst is almost inactive for NO_3^- reduction (Figure S8a,b).

The current density, normalized to the electrochemically active surface area (ECSA), increases exponentially to ∼1 mA cm^{-2} along with the cathodic potential for the case of $Cu_{50}Ni_{50}$. In contrast, an evident multi-electron-transfer process (Figure 2a,b) was seen on the pure Cu catalyst. $Cu_{50}Ni_{50}$ catalysts exhibited a 40% lower ECSA, determined by its double-layer capacitance, compared to pure Cu (Figure S9).

https://dx.doi.org/10.1021/jacs.9b13347
J. Am. Chem. Soc. XXXX, XXX, XXX−XXX

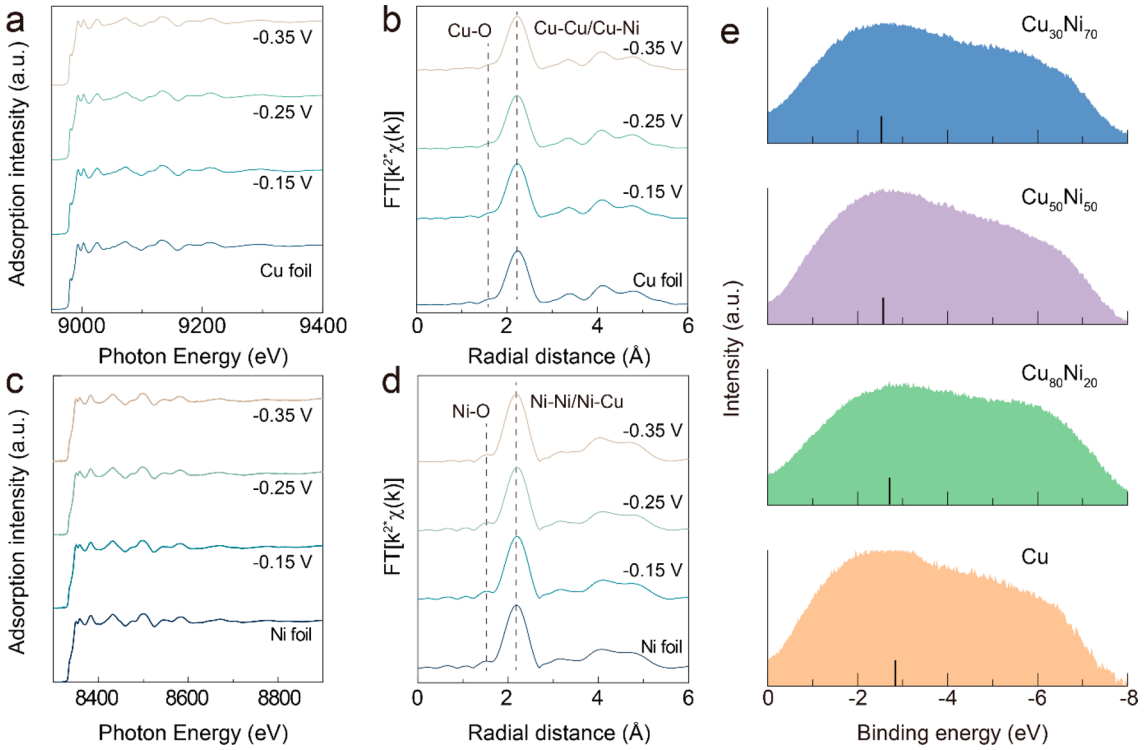

Figure 3. Electronic structure. (a) *Operando* Cu K-edge hXAS spectra of the $Cu_{50}Ni_{50}$ catalyst at different applied potentials. (b) Fourier-transformed *operando* Cu K-edge hXAS spectra of the $Cu_{50}Ni_{50}$ catalyst at different applied potentials. (c) *Operando* Ni K-edge hXAS spectra of the $Cu_{50}Ni_{50}$ catalyst at different applied potentials. (d) Fourier-transformed *operando* Ni K-edge hXAS spectra of the $Cu_{50}Ni_{50}$ catalyst at different applied potentials. (e) UPS spectra and *d*-band center positions of pure Cu catalysts and the CuNi alloys.

This translated to a 6-fold increase in ECSA-normalized current density for $Cu_{50}Ni_{50}$, compared to pure Cu at 0 V vs RHE (Figure 2b). The intrinsic NO_3^-RR activity was significantly improved using the CuNi alloy systems.

To gain insight into the kinetics, we plotted Koutecký–Levich (K-L) curves for NO_3^- reduction on the $Cu_{50}Ni_{50}$ and pure Cu catalysts (Figure 2c) using their current density vs potential (j–V) profiles in 1 M KOH + 10 mM KNO_3 (pH = 14) electrolyte (Figures S8c and S10). K-L analysis revealed a four-electron-transfer process for NH_3 production on both the $Cu_{50}Ni_{50}$ and Cu catalysts. The kinetic current density obtained using the $Cu_{50}Ni_{50}$ catalyst was calculated from the intercept of the K-L plot and was 220 mA cm^{-2} at −0.25 V vs RHE, 2 times higher than in the case of pure Cu controls (Table S2).

We investigated the $E_{1/2}$ of NO_3^-RR on catalysts with different Cu:Ni ratios in 1 M KOH + 10 mM KNO_3 electrolyte. On $Cu_{30}Ni_{70}$, $Cu_{50}Ni_{50}$, $Cu_{80}Ni_{20}$ alloys, we found increasing NO_3^-RR $E_{1/2}$ compared to the pure Cu catalyst. For instance, at 100 rpm, $Cu_{50}Ni_{50}$ catalyst exhibited the highest $E_{1/2}$ of 0.08 V vs RHE among all catalysts, while an $E_{1/2}$ of −0.045 V vs RHE was seen in the case of pure Cu (Figure S11). The improvement in $E_{1/2}$ further increased to ∼120 mV when catalysts were tested in 100 mM KNO_3 at the same rotating rate (Figure 2a). For all NO_3^- concentrations, $Cu_{50}Ni_{50}$ catalysts perform better than the pure Cu, as evidenced by the upshifting of $E_{1/2}$ and the reduced overpotential required for the same current density (Figure 2d and Figure S7d).

NO_3^-RR Selectivity. We investigated NH_3 selectivity using catalysts deposited on Cu/PTFE supports, e.g., the $Cu_{50}Ni_{50}$ catalyst on PTFE (labeled $Cu_{50}Ni_{50}$/PTFE), in a flow electrolyzer.[29] We quantified the NH_3 product concentration as a function of a range of NO_3^- concentrations using an indophenol blue method (Figure S12). To confirm that the NH_3 produced indeed comes from NO_3^- reduction, $^{15}NO_3^-$ electroreduction was performed using the same catalyst (Figure S13).

We achieved a 99 ± 1% Faradaic efficiency (FE) for NH_3 at ∼−0.15 V vs RHE on the $Cu_{50}Ni_{50}$/PTFE catalyst in 1 M KOH + 100 mM KNO_3 electrolyte (Figure 2e and Table S3). The peak FE for NH_3, on $Cu_{50}Ni_{50}$/PTFE, shifted to a 50 mV lower overpotential compared to that of the pure Cu/PTFE (Figure S14). The corresponding current density using $Cu_{50}Ni_{50}$/PTFE was more than 1.3 times higher than that obtained using pure Cu controls (Table S5). We checked for catalyst reconstruction following NO_3^- reduction after a 2-h NO_3^-RR operation in 100 mM NO_3^- and found that morphologies were retained in the case of both $Cu_{50}Ni_{50}$/PTFE and pure Cu/PTFE (Figure S15).

Alloying with Ni increased the NH_3 FE at low overpotentials (potentials > −0.1 V vs RHE) in different NO_3^- concentrations. $Cu_{50}Ni_{50}$ catalysts enhanced the NH_3 FE by over 20% at ∼0 V vs RHE compared to pure Cu (Figure 2f and Tables S4 and S5). Specifically, the highest NH_3 FEs are 65 ± 3%, 84 ± 2%, and 93 ± 2% in 1, 2, and 10 mM NO_3^- conditions at pH = 14, respectively. In contrast, pure Cu is only able to attain FEs of 42 ± 3%, 59 ± 3%, and 87 ± 3% at the same NO_3^- concentrations.

We achieved a peak NH_3 half-cell energy efficiency (EE) of 40% using $Cu_{50}Ni_{50}$/PTFE at 50 mA cm^{-2} in 100 mM NO_3^- (Figure 2g). This corresponds to a full-cell EE of 31% for this catalyst at 50 mA cm^{-2} in the same electrolyte (Figure S16), which is 1.3-fold improved compared to the case of the pure

https://dx.doi.org/10.1021/jacs.9b13347
J. Am. Chem. Soc. XXXX, XXX, XXX−XXX

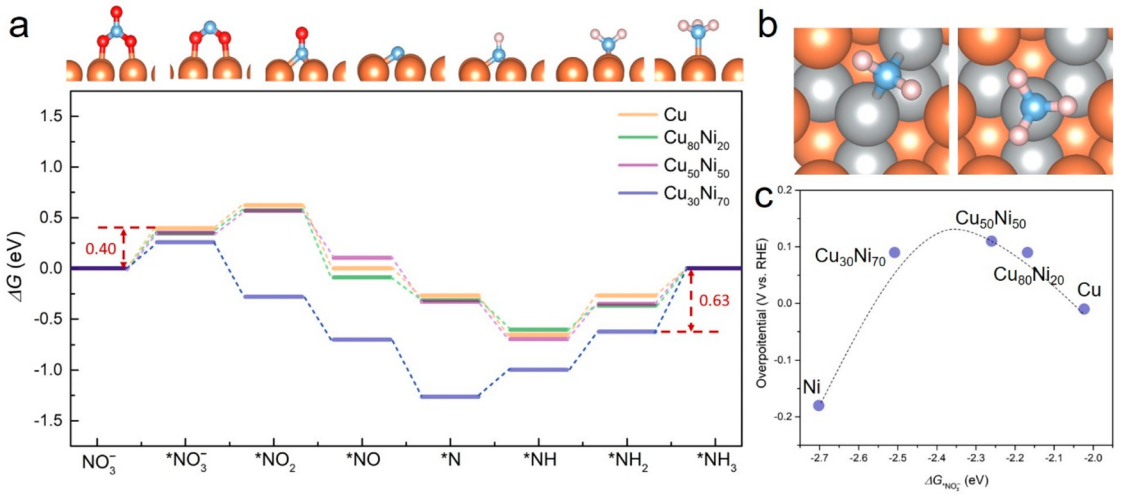

Figure 4. DFT calculations. (a) Reaction free energies for different intermediates on a CuNi surface. (b). Hydrogenation reaction of $*NH_2$ ($*NH_2 + H_2O + e^- \rightarrow *NH_3 + OH^-$) on a $Cu_{30}Ni_{70}$ surface. (c) The volcano-type relationship between experimental overpotentials of NO_3^-RR at 5 mA cm^{-2} in 10 mM KNO_3 and adsorption energies of $*NO_3^-$ on all CuNi alloys. Red, pink, blue, gray, and orange spheres correspond to oxygen, hydrogen, nitrogen, nickel, and copper atoms, respectively.

Cu catalyst. A 31% NH_3 full-cell EE was also obtained using $Cu_{50}Ni_{50}$/PTFE at 2 mA cm^{-2} in 2 mM NO_3^- (Figure S16). This is ∼6 times greater than that of the pure Cu catalyst under the same condition.

By studying both the NH_3 FE on $Cu_{80}Ni_{20}$ and $Cu_{30}Ni_{70}$ catalysts in 1 mM NO_3^-, we found that the $Cu_{50}Ni_{50}$ catalyst was the most active and selective catalyst (Figures S17 and 18). The NH_3 FE at −0.06 V vs RHE was 58 ± 2%. $Cu_{80}Ni_{20}$ catalysts produced NH_3 with a similar FE of 51 ± 2%. Introducing 70% Ni into Cu caused a sharp decrease in NH_3 FE from ∼58% to ∼31%. Depositing pure Ni largely blocked the Cu sites underneath and further reduced the NH_3 FE to 11 ± 1%.

We implemented the $Cu_{50}Ni_{50}$ catalyst on a 3D porous electrode by depositing the $Cu_{50}Ni_{50}$ catalyst onto a Cu foam with a pore size of ∼200 μm (Figure S19). We achieved, as a result, a 90 mA cm^{-2} current density at −0.1 V vs RHE, which is 2-fold higher than that obtained with the $Cu_{50}Ni_{50}$/PTFE electrode in 1 M KOH + 100 M KNO_3 (Figure 2h). The NH_3 FE was steady at ∼95% over 12 h of NO_3^-RR and at a 39% NH_3 half-cell EE. A total of 15% of the input NO_3^- was converted into NH_3 in a single pass (Figure 2h and Table S7).

Electronic Structure Studies. To shed light on the electronic structure of the CuNi alloy catalysts under NO_3^-RR conditions, we turned to *operando* hard XAS (hXAS).[30] The $Cu_{50}Ni_{50}$ catalyst in 1 M KOH + 10 mM KNO_3 electrolyte at a series of applied potentials exhibited pure metallic features in both Ni and Cu K-edge spectra under steady-state operation conditions (Figure 3a−d and Figure S20). We then calculated the *operando* coordination numbers (CNs) of Ni at different potentials. The CNs of metal−metal bonds stayed above 11.5 at all potentials (Tables S6 and S7). This result suggests that, in our work, there is unlikely to be a prominent role for subsurface oxygen species, as previously reported in related catalysts under distinct electrochemical (acidic) conditions.[31]

Since the adsorption energy of intermediates is strongly correlated with the *d*-band center position of catalysts,[32] we performed UPS studies for the pure Cu and the CuNi alloys (Figure 3e). The pure Cu catalyst exhibited a *d*-band center location of −2.84 eV ($E - E_F$, Fermi level) on the background-corrected spectrum. Increasing the Ni composition in the alloys causes an upshift of the *d*-band center toward the Fermi level by 0.14, 0.28, and 0.32 eV for $Cu_{80}Ni_{20}$, $Cu_{50}Ni_{50}$, and $Cu_{30}Ni_{70}$, respectively. These results were in agreement with the XPS results, wherein we observed the 2p electron redistribution which leads to a positive shift of the Cu 3d band toward the Fermi level. This indicates decreasing *anti*-bonding occupation and stronger adsorbate bonding,[32] which means that alloying Ni with Cu greatly enhances the adsorption energies of intermediate species.

Taken together, the activity, selectivity, and *d*-band center positions allow us to reason that enhanced NO_3^-RR intermediate adsorption, arising due to the shifted *d*-band center position, improved the NO_3^-RR activity and selectivity on CuNi alloys. However, introducing an excess of Ni, i.e., the $Cu_{30}Ni_{70}$ catalyst, affected the reaction intermediates too strongly, which lowers the activity and selectivity.

DFT Studies. We sought to investigate, using DFT, the relationship between intermediate adsorption and the NO_3^-RR activity of different CuNi catalysts (Figure 4a). The stability of CuNi alloy systems was screened via doping Ni into Cu at various layers and distributions (Figures S21 and S22 and Table S8). Thermodynamics first force Ni atoms to replace the subsurface Cu when the Ni:Cu ratio is less than 1:1. The substitution takes place on Cu surfaces with a further increase in the ratio (Figure S22).

The electrochemical reaction $NO_3^- + 6H_2O + 8e^- \rightarrow NH_3 + 9OH^-$ was represented by a series of deoxidation reactions, $*NO_3^- \rightarrow *NO_2 \rightarrow *NO \rightarrow *N$, followed by hydrogenation reactions, $*N \rightarrow *NH \rightarrow *NH_2 \rightarrow *NH_3$, according to a previous report.[33] With the stable CuNi structures we built, we took into account different adsorbed orientations of intermediates on all possible active sites (Figures S23 and S24). For all intermediates, the most stable adsorption configurations (Figure 4a) with the lowest total energies were employed to illustrate the NO_3^-RR pathway, and hence assess the activities of different catalysts.

A full NO_3^-RR pathway in 1 M KOH (pH = 14), including the deoxidation/hydrogenation reactions and intermediates,[33] was then calculated (Figure 4a). On pure Cu, the first NO_3^-

https://dx.doi.org/10.1021/jacs.9b13347
J. Am. Chem. Soc. XXXX, XXX, XXX−XXX

adsorption step is the potential-dependent step (PDS), of which the maximum reaction free energy is 0.40 eV at −0.14 V vs standard hydrogen electrode (SHE). Introducing Ni atoms moves the PDS from NO_3^- adsorption to the hydrogenation of the $*NH_2$ intermediate ($*NH_2 + H_2O + e^- \rightarrow *NH_3 + OH^-$, Figure 4b), as the result of enhanced adsorption caused by the upshifted *d*-band center (Figure 3e). A volcano-type relationship between the $*NO_3^-$ adsorption energy and the NO_3^-RR experimental overpotentials was seen (Figure 4c). With increasing Ni concentration in CuNi alloys, a stronger adsorption of $*NO_3^-$ on the surface further modifies the energetics of NO_3^-RR. However, on $Cu_{30}Ni_{70}$ alloy and pure Ni, the reaction free energy for $*NH_2$ hydrogenation increases to −0.39 and −0.34 eV at −0.14 V vs SHE, as high Ni fractions lead to $*NH_2$ intermediate adsorptions exceeding the optimal values. This fact, along with a possible decrease in the number of Cu sites (Figures S23 and S24), works against the formation of $*NH_3$, and the selectivity toward NH_3 decreases as a result.

CONCLUSIONS

This work presents the relationship between intermediate adsorption energies and NO_3^-RR activity on CuNi catalysts. By replacing 50% Cu with Ni, we achieved significantly improved NO_3^-RR-to-NH_3 performance. This includes a 0.12 V upshift in the half-wave potential, a 0.2 V lower overpotential required to achieve the optimal NH_3 FE, and a 6-fold increase in NO_3^-RR activity on $Cu_{50}Ni_{50}$ alloy catalysts compared to the values obtained with pure Cu at 0 V vs RHE in alkaline conditions (pH = 14). The electronic structure studies revealed an upshifting of the *d*-band center toward the Fermi level, a feature that enhances intermediate adsorption energies. This relationship was then validated by our DFT calculations, wherein we found that introducing Ni atoms moves the PDS from NO_3^- adsorption to $*NH_2$ hydrogenation due to the enhanced adsorption energy of NO_3^- on the CuNi surface and, as a result, lowers the overpotential. Our work demonstrates the effect of the *d*-band center positions and the induced adsorption properties on the NO_3^-RR activity and selectivity. This work highlights a promising route to design catalysts for selective NO_3^-RR to NH_3 conversion.

ASSOCIATED CONTENT

Supporting Information

The Supporting Information is available free of charge at https://pubs.acs.org/doi/10.1021/jacs.9b13347.

Materials and methods; Figures S1−S24 and Tables S1−S8 (PDF)

AUTHOR INFORMATION

Corresponding Author

Edward H. Sargent − *Department of Electrical and Computer Engineering, University of Toronto, Toronto, Ontario M5S 3G4, Canada;* orcid.org/0000-0003-0396-6495; Email: ted.sargent@utoronto.ca

Authors

Yuhang Wang − *Department of Electrical and Computer Engineering, University of Toronto, Toronto, Ontario M5S 3G4, Canada;* orcid.org/0000-0001-5336-5183

Aoni Xu − *Department of Electrical and Computer Engineering, University of Toronto, Toronto, Ontario M5S 3G4, Canada*

Ziyun Wang − *Department of Electrical and Computer Engineering, University of Toronto, Toronto, Ontario M5S 3G4, Canada;* orcid.org/0000-0002-2817-8367

Linsong Huang − *Laboratory of Advanced Materials, Department of Chemistry, Fudan University, Shanghai 200438, China*

Jun Li − *Department of Electrical and Computer Engineering and Department of Mechanical and Industrial Engineering, University of Toronto, Toronto, Ontario M5S 3G4, Canada*

Fengwang Li − *Department of Electrical and Computer Engineering, University of Toronto, Toronto, Ontario M5S 3G4, Canada;* orcid.org/0000-0003-1531-2966

Joshua Wicks − *Department of Electrical and Computer Engineering, University of Toronto, Toronto, Ontario M5S 3G4, Canada*

Mingchuan Luo − *Department of Electrical and Computer Engineering, University of Toronto, Toronto, Ontario M5S 3G4, Canada*

Dae-Hyun Nam − *Department of Electrical and Computer Engineering, University of Toronto, Toronto, Ontario M5S 3G4, Canada;* orcid.org/0000-0002-0871-1355

Chih-Shan Tan − *Department of Electrical and Computer Engineering, University of Toronto, Toronto, Ontario M5S 3G4, Canada*

Yu Ding − *Laboratory of Advanced Materials, Department of Chemistry, Fudan University, Shanghai 200438, China*

Jiawen Wu − *Laboratory of Advanced Materials, Department of Chemistry, Fudan University, Shanghai 200438, China*

Yanwei Lum − *Department of Electrical and Computer Engineering, University of Toronto, Toronto, Ontario M5S 3G4, Canada*

Cao-Thang Dinh − *Department of Electrical and Computer Engineering, University of Toronto, Toronto, Ontario M5S 3G4, Canada;* orcid.org/0000-0001-9641-9815

David Sinton − *Department of Mechanical and Industrial Engineering, University of Toronto, Toronto, Ontario M5S 3G8, Canada;* orcid.org/0000-0003-2714-6408

Gengfeng Zheng − *Laboratory of Advanced Materials, Department of Chemistry, Fudan University, Shanghai 200438, China;* orcid.org/0000-0002-1803-6955

Complete contact information is available at: https://pubs.acs.org/10.1021/jacs.9b13347

Author Contributions

#Y.W., A.X., and Z.W. contributed equally to this work.

Notes

The authors declare no competing financial interest.

ACKNOWLEDGMENTS

This work was financially supported by the Ontario Research Fund - Research Excellence Program, the Natural Sciences and Engineering Research Council (NSERC) of Canada, and the CIFAR Bio-Inspired Solar Energy program. This research used synchrotron resources of the Advanced Photon Source (APS), an Office of Science User Facility operated for the U.S. Department of Energy (DOE) Office of Science by Argonne National Laboratory, and was supported by the U.S. DOE under Contract No. DE-AC02-06CH11357, and the Canadian Light Source and its funding partners. All DFT computations were performed on the IBM BlueGene/Q supercomputer with support from the Southern Ontario Smart Computing Innovation Platform (SOSCIP) and Niagara supercomputer

https://dx.doi.org/10.1021/jacs.9b13347
J. Am. Chem. Soc. XXXX, XXX, XXX−XXX

at the SciNet HPC Consortium. SOSCIP is funded by the Federal Economic Development Agency of Southern Ontario, the Province of Ontario, IBM Canada Ltd., Ontario Centres of Excellence, Mitacs, and 15 Ontario academic member institutions. SciNet is funded by the Canada Foundation for Innovation, the Government of Ontario, Ontario Research Fund - Research Excellence, and the University of Toronto. We acknowledge the Toronto Nanofabrication Centre (TNFC) and the Ontario Centre for the Characterization of Advanced Materials (OCCAM) for sample preparation and characterization facilities. The authors thank Dr. T. P. Wu and L. Ma for technical support at the 9BM beamline of APS. D.S. acknowledges the NSERC E.W.R. Steacie Memorial Fellowship. J.L. acknowledges the Banting postdoctoral fellowship from Govt. of Canada.

REFERENCES

(1) Gruber, N.; Galloway, J. N. An Earth-system perspective of the global nitrogen cycle. *Nature* **2008**, *451*, 293−296.
(2) Canfield, D. E.; Glazer, A. N.; Falkowski, P. G. The evolution and future of Earth's nitrogen cycle. *Science* **2010**, *330*, 192−196.
(3) Penn State. Clean Air Act Reduces Acid Rain in Eastern United States. *ScienceDaily*, September 28, 1998. https://www.sciencedaily.com/releases/1998/09/980928072644.htm
(4) NO_x/VOC office. *NOx/VOC somg fact sheet*, Canadian Council of Ministers of the Environment, Ottawa, ON, Canada, 1998. https://www.ccme.ca/files/Resources/air/emissions/pn_1257_e.pdf
(5) Moorcroft, M. J.; Davis, J.; Compton, R. G. Detection and determination of nitrate and nitrite: a review. *Talanta* **2001**, *54*, 785−803.
(6) Nolan, B. T.; Hitt, K. J.; Ruddy, B. C. Probability of nitrate contamination of recently recharged groundwaters in the conterminous United States. *Environ. Sci. Technol.* **2002**, *36*, 2138−2145.
(7) Ascott, M.; Gooddy, D. C.; Wang, L.; Stuart, M. E.; Lewis, M. A.; Ward, R. S.; Binley, A. M. Global patterns of nitrate storage in the vadose zone. *Nat. Commun.* **2017**, *8*, 1416.
(8) Ford, C. L.; Park, Y. J.; Matson, E. M.; Gordon, Z.; Fout, A. R. A bioinspired iron catalyst for nitrate and perchlorate reduction. *Science* **2016**, *354*, 741−743.
(9) Duca, M.; Koper, M. T. Powering denitrification: the perspectives of electrocatalytic nitrate reduction. *Energy Environ. Sci.* **2012**, *5*, 9726−9742.
(10) Rosca, V.; Duca, M.; de Groot, M. T.; Koper, M. T. Nitrogen cycle electrocatalysis. *Chem. Rev.* **2009**, *109*, 2209−2244.
(11) Seraj, S.; Kunal, P.; Li, H.; Henkelman, G.; Humphrey, S. M.; Werth, C. J. PdAu alloy nanoparticle catalysts: effective candidates for nitrite reduction in water. *ACS Catal.* **2017**, *7*, 3268−3276.
(12) Butcher, D. P.; Gewirth, A. A. Nitrate reduction pathways on Cu single crystal surfaces: Effect of oxide and Cl^-. *Nano Energy* **2016**, *29*, 457−465.
(13) Pérez-Gallent, E.; Figueiredo, M. C.; Katsounaros, I.; Koper, M. T. Electrocatalytic reduction of nitrate on copper single crystals in acidic and alkaline solutions. *Electrochim. Acta* **2017**, *227*, 77−84.
(14) Chen, J. G.; Crooks, R. M.; Seefeldt, L. C.; Bren, K. L.; Bullock, R. M.; Darensbourg, M. Y.; Holland, P. L.; Hoffman, B.; Janik, M. J.; Jones, A. K.; Kanatzidis, M. G.; King, P.; Lancaster, K. M.; Lymar, S. V.; Pfromm, P.; Schneider, W. F.; Schrock, R. R. Beyond fossil fuel-driven nitrogen transformations. *Science* **2018**, *360*, No. eaar6611.
(15) Reyter, D.; Chamoulaud, G.; Bélanger, D.; Roué, L. Electrocatalytic reduction of nitrate on copper electrodes prepared by high-energy ball milling. *J. Electroanal. Chem.* **2006**, *596*, 13−24.
(16) Reyter, D.; Bélanger, D.; Roué, L. Study of the electroreduction of nitrate on copper in alkaline solution. *Electrochim. Acta* **2008**, *53*, 5977−5984.
(17) Comisso, N.; Cattarin, S.; Fiameni, S.; Gerbasi, R.; Mattarozzi, L.; Musiani, M.; Vázquez-Gómez, L.; Verlato, E. Electrodeposition of Cu−Rh alloys and their use as cathodes for nitrate reduction. *Electrochem. Commun.* **2012**, *25*, 91−93.
(18) Mattarozzi, L.; Cattarin, S.; Comisso, N.; Gambirasi, A.; Guerriero, P.; Musiani, M.; Vázquez-Gómez, L.; Verlato, E. Hydrogen evolution assisted electrodeposition of porous Cu-Ni alloy electrodes and their use for nitrate reduction in alkali. *Electrochim. Acta* **2014**, *140*, 337−344.
(19) Mattarozzi, L.; Cattarin, S.; Comisso, N.; Guerriero, P.; Musiani, M.; Vázquez-Gómez, L.; Verlato, E. Electrochemical reduction of nitrate and nitrite in alkaline media at CuNi alloy electrodes. *Electrochim. Acta* **2013**, *89*, 488−496.
(20) Simpson, B. K.; Johnson, D. C. Electrocatalysis of nitrate reduction at copper-nickel alloy electrodes in acidic media. *Electroanalysis* **2004**, *16*, 532−538.
(21) Stamenković, V. R.; Schmidt, T. J.; Ross, P. N.; Marković, N. M. Surface composition effects in electrocatalysis: kinetics of oxygen reduction on well-defined Pt_3Ni and Pt_3Co alloy surfaces. *J. Phys. Chem. B* **2002**, *106*, 11970−11979.
(22) Stamenković, V. R.; Fowler, B.; Mun, B. S.; Wang, G.; Ross, P. N.; Lucas, C. A.; Marković, N. M. Improved oxygen reduction activity on $Pt_3Ni(111)$ via increased surface site availability. *Science* **2007**, *315*, 493−499.
(23) Nørskov, J. K.; Rossmeisl, J.; Logadottir, A.; Lindqvist, L.; Kitchin, J. R.; Bligaard, T.; Jonsson, H. Origin of the overpotential for oxygen reduction at a fuel-cell cathode. *J. Phys. Chem. B* **2004**, *108*, 17886−17892.
(24) Huang, H.; Jia, H.; Liu, Z.; Gao, P.; Zhao, J.; Luo, Z.; Yang, J.; Zeng, J. Understanding of strain effects in the electrochemical reduction of CO_2: using Pd nanostructures as an ideal platform. *Angew. Chem., Int. Ed.* **2017**, *56*, 3594−3598.
(25) Kim, D.; Resasco, J.; Yu, Y.; Asiri, A. M.; Yang, P. Synergistic geometric and electronic effects for electrochemical reduction of carbon dioxide using gold−copper bimetallic nanoparticles. *Nat. Commun.* **2014**, *5*, 4948.
(26) Theivasanthi, T.; Alagar, M. X-ray diffraction studies of copper nanopowder. *arXiv (General Physics)*, March 31, 2010, 1003.6068. https://arxiv.org/abs/1003.6068
(27) Jha, A.; Jeong, D.-W.; Shim, J.-O.; Jang, W.-J.; Lee, Y.-L.; Rode, C. V.; Roh, H.-S. Hydrogen production by the water-gas shift reaction using $CuNi/Fe_2O_3$ catalyst. *Catal. Sci. Technol.* **2015**, *5*, 2752−2760.
(28) Hsieh, H. H.; Chang, Y. K.; Pong, W. F.; Pieh, J. Y.; Tseng, P. K.; Sham, T. K.; Coulthard, I.; Naftel, S. J.; Lee, J. F.; Chung, S. C.; Tsang, K. L. Electronic structure of Ni-Cu alloys: the *d*-electron charge distribution. *Phys. Rev. B: Condens. Matter Mater. Phys.* **1998**, *57*, 15204−15210.
(29) Dinh, C.-T.; Burdyny, T.; Kibria, M. G.; Seifitokaldani, A.; Gabardo, C. M.; Garcia de Arquer, F. P.; Kiani, A.; Edwards, J. P.; De Luna, P.; Bushuyev, O. S.; Zou, C.; Quintero-Bermudez, R.; Pang, Y.; Sinton, D.; Sargent, E. H. CO_2 electroreduction to ethylen via hydroxide-mediated copper catalysis at an abrupt interface. *Science* **2018**, *360*, 783−787.
(30) Li, J.; Che, F.; Pang, Y.; Zou, C.; Howe, J. Y.; Burdyny, T.; Edwards, J. P.; Wang, Y.; Li, F.; Wang, Z.; De Luna, P.; Dinh, C.-T.; Zhuang, T.-T.; Saidaminov, M. I.; Cheng, S.; Wu, T.; Finfrock, Y. Z.; Ma, L.; Hsieh, S.-H.; Liu, Y.-S.; Botton, G. A.; Pong, W.-F.; Du, X.; Guo, J.; Sham, T.-K.; Sargent, E. H.; Sinton, D. Copper adparticle enabled selective electrosynthesis of n-propanol. *Nat. Commun.* **2018**, *9*, 4614.
(31) Bae, S.-E.; Stewart, K. L.; Gewirth, A. A. Nitrate adsorption and reduction on Cu(100) in acidic solution. *J. Am. Chem. Soc.* **2007**, *129*, 10171−10180.
(32) Nørskov, J. K.; Abild-Pedersen, F.; Studt, F.; Bligaard, T. Density functional theory in surface chemistry and catalysis. *Proc. Natl. Acad. Sci. U. S. A.* **2011**, *108*, 937−943.
(33) Liu, J.-X.; Richards, D.; Singh, N.; Goldsmith, B. R. Activity and Selectivity Trends in electrocatalytic nitrate reduction on transition metals. *ACS Catal.* **2019**, *9*, 7052−7064.

https://dx.doi.org/10.1021/jacs.9b13347
J. Am. Chem. Soc. XXXX, XXX, XXX−XXX